A survey of molecular line emission towards Herbig Be star V645 Cyg

Monthly Notices of the ROYAL ASTRONOMICAL SOCIETY

MNRAS **528,** 108–121 (2024) https://doi.org/10.1093/mnras/stad3947
Advance Access publication 2023 December 22

A survey of molecular line emission towards Herbig Be star V645 Cyg

A. D. Gimalieva [1]★ M. S. Kirsanova [1,2] S. V. Salii,[1] S. V. Kalenskii,[3] A. O. H. Olofsson[4] and A. P. Topchieva [2]

[1]*Institute of Natural Sciences and Mathematics, Ural Federal University, 19 Mira Str, Ekaterinburg 620075, Russia*
[2]*Institute of Astronomy, Russian Academy of Sciences, 48 Pyatnitskaya Str, Moscow 119017, Russia*
[3]*Astro Space Center, Lebedev Physical Institute, Russian Academy of Sciences, 84/32 Profsoyuznaya Str, Moscow 117997, Russia*
[4]*Department of Space, Earth and Environment, Chalmers University of Technology, Onsala Space Observatory, SE-43992 Onsala, Sweden*

Accepted 2023 December 19. Received 2023 December 19; in original form 2023 September 29

ABSTRACT

We present a survey of molecular line emission towards the molecular cloud surrounding Herbig Be star V645 Cyg. The survey was performed with the 20-m Onsala space telescope at 3 and 4 mm. We detected emission lines of 33 molecules and their isotopologues from diatomic molecules to four COMs up to seven atoms. Using detected lines, we estimated molecular column densities and abundances relative to molecular hydrogen in local thermodynamic equilibrium (LTE) approximation for all molecules except for methanol, for which we obtained physical parameters using a non-LTE model. Moreover, in the basement of the non-LTE model of methanol line emission, we consider that there is a weak maser effect in the additional spectral component of 5_1–4_0 E methanol line at 84.521 GHz. We compared the molecular abundances with values found in several astrochemical templates: molecular clouds, hot cores, and photodissociation regions, and found that signatures of these different types can be found towards V645 Cyg. We also obtained maps of the cloud in several molecular emission lines. The peaks of CO and CH_3OH emission are shifted from the direction of the star, but the CS, HCO^+, HNC, HCN, and N_2H^+ emission peaks are observed directly towards the star. Exploring the gas kinematics around V645 Cyg, we found that velocity structure in the ambient molecular cloud on the scale ≈1.6–2.0 pc is not the same as within ≈0.5 pc found previously by other authors.

Key words: masers – stars: variables: T Tauri, Herbig Ae/Be – ISM: abundances – ISM: clouds – ISM: individual objects: V645 Cyg – ISM: molecules.

1 INTRODUCTION

Astrochemical studies of star-forming objects started in the middle of the last century. Since that time, researchers have found several astrochemical patterns that refer to different types of objects, e.g. low-mass dark starless clouds (e.g. TMC 1; see Cernicharo et al. 2011), hot cores in massive star-forming regions (e.g. G31.41+0.31; see Rivilla et al. 2017), and photodissociation regions (PDRs) for material irradiated by ultraviolet (UV) emission (e.g. the Orion Bar PDR; Cuadrado et al. 2017). Environments of Herbig Ae/Be stars represent potentially a mixture of several templates, because UV-driven chemistry can go along with the high-temperature chemical reactions in the molecular gas of parental clouds. While many studies of the chemistry around Herbig Ae/Be stars targeted their immediate environment, namely, circumstellar discs (see e.g. recent studies by Smirnov-Pinchukov et al. 2022; Pegues et al. 2023), there are extended molecular clouds around such objects. Our aim is to understand which typical chemical pattern or their mixture matches these clouds.

For our study, we selected a star-like object, V645 Cyg, which is representative of a rare class of objects situated at the distance of 4.5 kpc from the Sun (Reid et al. 2019). This is a bright Herbig Be star (Miroshnichenko et al. 2009), surrounded by extended optical nebulosity. Sandell, Weintraub & Hamidouche (2011) observed submillimetre emission towards V645 Cyg and found that the star is still partly embedded in the parental molecular cloud ridge, with a mass for the densest part of 85 $M_\odot$. A bipolar molecular outflow coaligned with optical outflow is observed within the 15 arcsec around the star (see Goodrich 1986; Verdes-Montenegro et al. 1991; Acke, van den Ancker & Dullemond 2005; Eisner et al. 2015; Pomohaci, Oudmaijer & Goodwin 2019). Radio continuum emission from an H II region excited by V645 Cyg and the ionized outflow was found by Skinner, Brown & Stewart (1993) and Girart et al. (2002).

V645 Cyg demonstrates variable emission in a broad range of wavelengths. Girart et al. (2002) found that variable centimetre radio continuum emission is probably related to the episodic ejection of material by the star. Variable centimetre and millimetre maser emission (e.g. Slysh et al. 1999, 2002; Szymczak, Hrynek & Kus 2000; Błaszkiewicz & Kus 2004; Aberfelds et al. 2023) is associated with outflow activity or radial velocity drift in a circumstellar disc surrounding the star (see also Bae et al. 2011). Hamann & Persson (1989) found signatures of a stellar wind activity in the optical spectra of the star. Shevchenko et al. (1994) and Miroshnichenko et al. (2009) reported the variable irregular optical emission of the

★ E-mail: alina.gimalieva@mail.ru

star. Clarke et al. (2006) found evidence of variable stellar wind in V645 Cyg from hydrogen recombination lines and outflow with CO bandhead emission and suggested rapidly expanding photosphere in this object. Gorda et al. (2022) related a monotonous part of the optical variability due to release of surrounding material.

In spite of the long-term history of research, not much attention has been paid to molecular composition of the material around V645 Cyg. Several bright lines of CO, CS, SiO, N_2H^+, HCN, and CCH at 3 mm were detected towards this object via surveys of molecular emission in masers, outflows, and early-type stars with single-dish telescopes by Harju et al. (1998), Scappini et al. (1998), Larionov et al. (1999), Liu et al. (2011), and Shakhvorostova et al. (2023). Being a part of a large program CORE (Beuther et al. 2018), the star was observed at 1.3 mm using the NOrthern Extended Millimeter Array (NOEMA), and complex molecules such as CH_3OH and CH_3CN were detected by Gieser et al. (2021) in the immediate vicinity of the star.

We performed a line survey of V645 Cyg at 3 and 4 mm in order to study the transformation of residual molecular gas around this young Herbig Be star under the influence of the outflow, high temperature, and UV radiation, and made maps in selected lines.

2 OBSERVATIONS

With the Onsala Space Observatory 20-m telescope in 2016 December, 2017 February, and 2019 March the survey was performed towards $\alpha = 21^{\rm h}39^{\rm m}58\overset{\rm s}{.}9$, $\delta = 50^\circ14'24''$ (J2000), corresponding to a Class II methanol maser found by Slysh et al. (1999) in V645 Cyg. The maps were centred towards the same position. In all observational periods we used a dual polarization sideband separating receiver (Belitsky et al. 2015). The backend used was a FFTs in 2 × 2.5 GHz mode (spectral interval centres being separated by 12 GHz), providing a spectral resolution of 76 kHz. We mapped emission in the CS(2–1), ^{13}CO(1–0), C^{18}O(1–0), C^{34}S(1–0), HCO^+(1–0), HCN(1–0), HNC(1–0), N_2H^+(1–0), and $CH_3OH(2_K–1_K)$ lines using a raster mapping method with a step size of 20 arcsec. The telescope beam size varies with frequency: from 40 arcsec for the N_2H^+(1–0) to 34 arcsec for the ^{13}CO(1–0) line. The maps were done in the frequency-switch mode with a 5 MHz frequency offset. For the survey, we started from 72 GHz and moved up to 110 GHz (except of a 78–83 GHz frequency range) in the dual-beam-switch mode, providing the best baseline. Conversion from antenna temperature to main beam temperature $T_{\rm mb}$ was made with the beam efficiency coefficient $\nu_{\rm mb}$, depending on the source elevation, e.g. $\nu_{\rm mb} = 0.4$ at 100 GHz for the 47° elevation value (see Belitsky et al. 2015).

Telescope pointing and focusing accuracy was checked using SiO maser lines in R Cas and χ Cyg sources after sunrise and sunset. Average focus accuracy was ≈0.6, 0.5, and 0.53 mm, pointing accuracy was ≈3.7/2.5, 1.8/1.6, 3.8/4.4 arcsec in azimuth and elevation in the 2016, 2017, and 2019 observation sessions, respectively.

Typical system temperature varied from 200 to 300 K but sometimes was as high as 400 K in the case of bad weather. The noise level of our data is 10–20 mK in the $T_{\rm mb}$ scale for the selected spectral resolution.

Data were reduced and analysed with the GILDAS[1] software.

[1]http://www.iram.fr/IRAMFR/GILDAS

3 METHODS

3.1 Analysis of the observed molecular lines

3.1.1 Optically thin lines

We found many emission lines, which appear only in dense gas (see Section 4.1), hence we used the local thermodynamic equilibrium (LTE) approximation for the data analysis of the environment of V645 Cyg.

Neglecting the background temperature and using Rayleigh–Jeans approximation, we can estimate molecular column densities with the following equation:

$$N = \frac{N_{\rm u}}{g_{\rm u}} Q_{\rm rot} \exp \frac{E_{\rm u}}{kT_{\rm ex}} \left({\rm cm}^{-2}\right), \quad (1)$$

where $Q_{\rm rot}$ value is the rotation–spin partition function at the excitation temperature $T_{\rm ex}$, $E_{\rm u}/k$ is the energy of the upper level of the transition in Kelvin (K). The $N_{\rm u}/g_{\rm u}$ ratio is the number density at the upper level of the transition divided by the upper level degeneracy:

$$\frac{N_{\rm u}}{g_{\rm u}} = \frac{3k}{8\pi^3} \frac{\int T_{\rm mb}\,{\rm d}V}{\nu S\mu^2} \left({\rm cm}^{-2}\right), \quad (2)$$

where $\int T_{\rm mb}\,{\rm d}V$ is the integrated intensity of the line and ν is the transition frequency. These values are given in Table 1, $S\mu^2$ is the product of the line strength and the squared permanent dipole moment. For non-linear molecules we used a power function interpolation of $Q_{\rm rot}$ values corresponding to particular temperature values that are held in the Jet Propulsion Laboratory (JPL) data base (Pickett et al. 1998):

$$Q_{\rm rot} = a\,T^b, \quad (3)$$

where a and b are constant.

For linear molecules, we adopted the following expression:

$$Q_{\rm rot} = \frac{k\,T_{\rm ex}}{h\,B} + \frac{1}{3}, \quad (4)$$

where B is the rotational constant. From those molecules, where we can estimate excitation temperature using rotational diagram analysis (CH_3CCH), we used the obtained value for equation (1). We used dust temperature $T_{\rm d} = 38$ K determined in Sandell et al. (2011) as the $T_{\rm ex}$ value if we could not estimate it analysing emission lines from isotopologues of particular molecule.

3.1.2 Optically thick lines

For pairs of molecules isotopologues (CS and C^{34}S, ^{13}CO and C^{18}O, HCO^+ and $H^{13}CO^+$, HCN and H^{13}CN, HNC and H^{13}NC) we used equation (5) to estimate optical depth of the more abundant molecules. Given low abundances of isotopologues, it is reasonable to assume that the associated lines can be considered as optically thin, therefore

$$\frac{T_{\rm thick}}{T_{\rm thin}} = \frac{1 - \exp\left(-\tau\right)}{1 - \exp\left(-\tau/\alpha\right)}, \quad (5)$$

where $T_{\rm thin}$ and $T_{\rm thick}$ are the main beam temperatures of the optically thin and thick lines, respectively.

The α value is the ratio of particular isotopes at the galactocentric distance of V645 Cyg (9.5 kpc). We took $\alpha = 71.1$ for ^{12}C/^{13}C, 554 for ^{16}O/^{18}O, and 22.5 for ^{32}S/^{34}S using values summarized by Wilson (1999). With the known τ we could estimate the excitation

Table 1. Detected molecular lines.

Molecule	Transition	Frequency (MHz)	E_u (K)	$\int T_{mb}\,dV$ (K km s^{-1})	V_{LSR} (km s^{-1})	ΔV (km s^{-1})	T_{mb} (K)
		Diatomic molecules					
CS	2–1	97980.953	7.1	7.30 ± 0.06	−44.00 ± 0.01	2.55 ± 0.03	2.69 ± 0.04
^{13}CS	2–1	92494.308	7.1	0.16 ± 0.01	−44.02 ± 0.06	1.7 ± 0.13	0.08 ± 0.01
C^{34}S	2–1	96412.950	7.1	0.53 ± 0.03	−44.01 ± 0.05	2.03 ± 0.13	0.24 ± 0.02
^{13}CO	1–0	110201.354	5.3	29.23 ± 0.22	−43.93 ± 0.01	2.51 ± 0.02	10.94 ± 0.27
C^{18}O	1–0	109782.176	5.3	3.88 ± 0.05	−43.95 ± 0.01	2.0.7 ± 0.03	1.76 ± 0.05
^{13}C^{18}O	1–0	104711.403	5.3	0.06 ± 0.01	−44.34 ± 0.17	1.48 ± 0.44	0.04 ± 0.01
SiO	2–1	86846.960	6.3	0.10 ± 0.01	−44.43 ± 0.19	3.02 ± 0.44	0.03 ± 0.01
SO	3(2)–2(1)	99299.870	9.2	2.06 ± 0.02	−44.13 ± 0.01	2.21 ± 0.03	0.88 ± 0.03
SO	2(3)–1(2)	109252.220	21.1	0.19 ± 0.05	−43.51 ± 0.25	1.82 ± 0.40	0.10 ± 0.05
SO_2	8(3, 5)–9(2, 8)	86639.088	55.2				<0.03
SO_2	3(1, 3)–2(0, 2)	104029.418	7.7	0.12 ± 0.01	−44.38 ± 0.23	2.96 ± 0.01	0.04 ± 0.01
		Triatomic molecules					
CCH	N = 1–0, J = 3/2–1/2, F = 1–1	87284.156	4.2	0.25 ± 0.01	−43.94 ± 0.06	2.26 ± 0.13	0.10 ± 0.01
	N = 1–0, J = 3/2–1/2, F = 2–1	87316.925	4.2	2.03 ± 0.02	−43.93 ± 0.01	2.45 ± 0.03	0.78 ± 0.02
	N = 1–0, J = 3/2–1/2, F = 1–0	87328.624	4.2	1.04 ± 0.02	−43.91 ± 0.02	2.42 ± 0.05	0.40 ± 0.01
	N = 1–0, J = 1/2–1/2, F = 1–1	87402.004	4.2	1.04 ± 0.02	−43.95 ± 0.02	2.37 ± 0.05	0.41 ± 0.01
	N = 1–0, J = 1/2–1/2, F = 0–1	87407.165	4.2	0.44 ± 0.03	−44.02 ± 0.06	2.25 ± 0.15	0.18 ± 0.02
	N = 1–0, J = 1/2–1/2, F = 1–0	87446.512	4.2	0.24 ± 0.01	−43.92 ± 0.06	2.29 ± 0.14	0.10 ± 0.01
CCS	N = 7–6, J = 8–7	93870.107	10.7	0.12 ± 0.02	−44.17 ± 0.25	2.87 ± 0.49	0.04 ± 0.01
	N = 8–7, J = 9–8	106347.740	24.9	0.08 ± 0.02	−44.27 ± 0.20	1.51 ± 0.35	0.05 ± 0.02
N_2H^+	J = 1–0	93173.398	4.5	3.39 ± 0.2	−44.07 ± 0.01	2.60 ± 0.01	1.23 ± 0.02
HCO	1(0, 1)–0(0, 0), J = 3/2–1/2, F = 2–1	86670.760	4.2	0.09 ± 0.01	−44.18 ± 0.13	2.19 ± 0.34	0.04 ± 0.01
	1(0, 1)–0(0, 0), J = 3/2–1/2, F = 1–0	86708.360	4.2	0.06 ± 0.01	−43.74 ± 0.28	2.41 ± 0.53	0.02 ± 0.01
HCO^+	J = 1–0	89188.524	4.3	15.73 ± 0.15	−43.85 ± 0.01	3.07 ± 0.04	4.81 ± 0.17
$H^{13}CO^+$	J = 1–0	86754.288	4.2	1.55 ± 0.01	−44.05 ± 0.01	2.02 ± 0.02	0.72 ± 0.01
$HC^{17}O^+$	J = 1–0	87057.534	4.2	0.03 ± 0.01	−42.86 ± 0.13	1.02 ± 0.02	0.03 ± 0.01
DCO^+	J = 1–0	72039.312	3.5	0.76 ± 0.10	−44.06 ± 0.17	2.65 ± 0.37	0.27 ± 0.05
HCN	J = 1–0, F = 1–1	88630.416	4.3	3.67 ± 0.06	−44.07 ± 0.01	2.92 ± 0.06	1.18 ± 0.04
	J = 1–0, F = 2–1	88631.840	4.3	6.87 ± 0.06	−44.07 ± 0.01	2.64 ± 0.03	2.45 ± 0.04
	J = 1–0, F = 0–1	88633.936	4.3	1.48 ± 0.05	−44.07 ± 0.01	2.40 ± 0.10	0.58 ± 0.04
$H^{13}CN$	J = 1–0, F = 1–1	86338.735	4.1	0.22 ± 0.01	−43.90 ± 0.03	2.23 ± 0.17	0.09 ± 0.01
	J = 1–0, F = 2–1	86340.166	4.1	0.35 ± 0.01	−43.90 ± 0.03	2.00 ± 0.10	0.16 ± 0.01
	J = 1–0, F = 0–1	86342.254	4.1	0.08 ± 0.02	−43.90 ± 0.03	3.01 ± 0.79	0.02 ± 0.01
HNC	1–0	90663.568	4.3	7.18 ± 0.03	−43.98 ± 0.01	2.47 ± 0.01	2.73 ± 0.04
$HN^{13}C$	1–0	87090.850	4.2	0.30 ± 0.01	−43.93 ± 0.04	1.95 ± 0.10	0.15 ± 0.01
$H^{15}NC$	1–0	88865.715	4.3	0.10 ± 0.02	−43.83 ± 0.22	2.26 ± 0.43	0.04 ± 0.01
DCN	J = 1–0	72414.694	3.3	0.34 ± 0.08	−44.74 ± 0.39	2.44 ± 0.01	0.13 ± 0.05
DNC	J = 1–0	76305.727	3.7	0.29 ± 0.05	−43.84 ± 0.16	1.79 ± 0.43	0.15 ± 0.03
		Four atoms molecules					
para-H_2CO	$1_{(0,1)}$–$0_{(0,0)}$	72837.948	3.5	2.66 ± 0.09	−44.07 ± 0.04	2.55 ± 0.11	0.98 ± 0.07
	$6_{(1,5)}$–$6_{(1,6)}$	101332.991	87.6	0.04 ± 0.01	−43.49 ± 0.19	1.30 ± 0.01	0.03 ± 0.02
ortho-H_2CS	$3_{(1,3)}$–$2_{(1,2)}$	101477.810	22.9	0.21 ± 0.02	−44.59 ± 0.08	1.76 ± 0.18	0.11 ± 0.02
	$3_{(0,3)}$–$2_{(0,2)}$	103040.452	9.9	0.08 ± 0.02	−43.98 ± 0.24	1.61 ± 0.55	0.05 ± 0.01
	$3_{(1,2)}$–$2_{(1,1)}$	104617.040	23.2	0.21 ± 0.02	−44.07 ± 0.07	1.94 ± 0.18	0.10 ± 0.01
HNCO	4(0, 4)–3(0, 3)	87925.237	10.5	0.14 ± 0.01	−44.12 ± 0.08	2.07 ± 0.20	0.06 ± 0.01
	5(0, 5)–4(0, 4)	109905.749	15.8	0.18 ± 0.05	−44.76 ± 0.23	1.78 ± 0.49	0.10 ± 0.04
		Five atoms molecules					
ortho-c-C_3H_2	2(1, 2)–1(0, 1)	85338.894	6.4	0.72 ± 0.10	−43.68 ± 0.15	2.13 ± 0.35	0.32 ± 0.09
HC_3N	10–9	90979.023	24.0	0.91 ± 0.02	−43.99 ± 0.02	2.27 ± 0.04	0.38 ± 0.01
	11–10	100076.392	28.8	0.87 ± 0.01	−44.01 ± 0.02	2.14 ± 0.04	0.38 ± 0.01
	12–11	109173.634	34.1	0.79 ± 0.06	−44.01 ± 0.09	2.56 ± 0.22	0.29 ± 0.03

temperature and use it to calculate column density using

$$T_{ex} = \frac{T_{mb}}{1 - \exp(-\tau)}. \quad (6)$$

We expect a particular T_{ex} value for all the other detected molecular lines based on the assumption of chemical association of molecules or similar excitation conditions, e.g. we suppose the same T_{ex} for DCO^+ and HCO^+, N_2H^+ and HCN etc., see the details in Table 2.

Table 1. (Continued.).

Molecule	Transition	Frequency (MHz)	E_u (K)	$\int T_{mb}\,dV$ (K km s^{-1})	V_{LSR} (km s^{-1})	ΔV (km s^{-1})	T_{mb} (K)
			Six atoms molecules				
CH_3OH	5_{-1}–4_0 E	84521.172	40.4	0.17 ± 0.03	-43.86 ± 0.27	3.16 ± 0.75	0.05 ± 0.01
	6_{-2}–7_{-1} E	85568.131	74.7				$\leq$0.05
	7_2–6_3 A^{--}	86615.574	102.7				$\leq$0.02
	8_0–7_1 A^{++}	95169.391	83.5				$\leq$0.02
	2_1–1_1 A^{++}	95914.310	21.4				$\leq$0.02
	2_{-1}–1_{-1} E	96739.358	12.5	1.10 ± 0.04	-43.99 ± 0.03	3.04 ± 0.14	0.34 ± 0.03
	2_0–1_0 A^{++}	96741.371	7.0	1.42 ± 0.04	-43.99 ± 0.03	2.78 ± 0.09	0.48 ± 0.03
	2_0–1_0 E	96744.545	20.1	0.18 ± 0.04	-43.99 ± 0.03	2.42 ± 0.67	0.07 ± 0.03
	2_1–1_1 E	96755.501	28.0				<0.02
	2_1–1_1 A^{--}	97582.798	21.6				<0.04
	3_1–4_0 A^{++}	107013.831	28.3				<0.02
	0_0–1_1 E	108893.945	13.1				$\leq$0.05
CH_3CN	5_3–4_3 E	91971.130	77.6				$\leq$0.01
	5_2–4_2 E	91979.994	41.8	0.07 ± 0.01	-43.68 ± 0.17	5.56 ± 1.18	0.02 ± 0.01
	5_1–4_1 E	91985.314	20.4	0.07 ± 0.01	-43.68 ± 0.17	2.64 ± 0.50	0.03 ± 0.01
	5_0–4_0 A	91987.087	13.2	0.09 ± 0.01	-43.68 ± 0.17	3.20 ± 0.60	0.03 ± 0.01
			Seven atoms molecules				
CH_3CCH	5_3–4_3	85442.528	77.3				<0.05
	5_2–4_2	85450.730	41.2				<0.05
	5_1–4_1	85455.622	19.5	0.15 ± 0.06	-44.05 ± 0.16	1.65 ± 0.01	0.09 ± 0.05
	5_0–4_0	85457.272	12.3	0.35 ± 0.07	-44.05 ± 0.16	1.69 ± 0.32	0.19 ± 0.05
	6_3–5_3	102530.349	82.0	0.05 ± 0.01	-43.92 ± 0.04	1.70 ± 0.01	0.03 ± 0.01
	6_2–5_2	102540.145	46.0	0.10 ± 0.02	-43.92 ± 0.04	1.69 ± 0.31	0.05 ± 0.01
	6_1–5_1	102546.024	24.4	0.27 ± 0.02	-43.92 ± 0.04	2.34 ± 0.19	0.11 ± 0.01
	6_0–5_0	102547.984	17.2	0.33 ± 0.02	-43.92 ± 0.04	1.83 ± 0.10	0.17 ± 0.01
CH_3CHO	$5_{(1,5)}$–$4_{(1,4)}$ E	93595.235	15.8	0.03 ± 0.01	-43.88 ± 0.20	1.30 ± 0.01	0.03 ± 0.01
	$5_{(0,5)}$–$4_{(0,4)}$ E	95947.437	13.9	0.07 ± 0.02	-43.47 ± 0.31	2.39 ± 0.94	0.03 ± 0.01
	$5_{(0,5)}$–$4_{(0,4)}$ A	95963.459	13.8	0.05 ± 0.02	-44.00 ± 0.19	1.23 ± 0.44	0.04 ± 0.01
	$5_{(1,4)}$–$4_{(1,3)}$ E	98863.313	16.6				$\leq$0.01
	$5_{(1,4)}$–$4_{(1,3)}$ A	98900.944	16.5				$\leq$0.02
			Unidentified lines				
		80586.423		0.12 ± 0.02	-42.13 ± 0.14	1.30 ± 0.01	0.09 ± 0.02
		96300.450		0.56 ± 0.05	-43.45 ± 0.11	2.84 ± 0.31	0.19 ± 0.03
		102608.586		0.34 ± 0.02	-43.75 ± 0.07	2.27 ± 0.18	0.14 ± 0.01
		108520.202		0.53 ± 0.05	-45.30 ± 0.16	3.13 ± 0.37	0.16 ± 0.03

Considering the optical depth τ of the main isotopologues, we calculated their column density as $N \times \tau/(1 - \exp(-\tau))$.

3.1.3 LVG approximation

Using the large velocity gradient (LVG) approximation, we estimated physical conditions that produce the observed methanol emission at 84–109 GHz frequency band. In order to do this, we used a pre-compiled data base by Salii, Parfenov & Sobolev (2018). This data base contains the population numbers for quantum energy levels of methanol of ground and torsionally excited levels with v_t up to 2. Data base parameters are varied from 10 to 600 K for T_k, from 3.0 to 9.0 for $\lg(n_{H_2})$, from 7.5 to 14.0 for $\lg(N_{CH_3OH}/\Delta V)$, from -9.0 to -5.5 for $\lg(N_{CH_3OH}/N_{H_2})$, at 1, 3, and 5 km s^{-1} for ΔV. For the purpose of getting better model intensities we varied a beam filling factor from 10 to 100 per cent. Details of the LVG calculation were published in Kirsanova et al. (2021a).

We found out the model that provides the best coincidence between the modelled and observed line intensities (with χ^2 minimum). For undetected lines of methanol it was controlled that their model intensities not exceed the rms level from Table 1. Here we used a fixed line width of 3 km s^{-1} for all methanol lines since this is the closest value to the observed full width at half-maximum (FWHM) given in Table 1.

3.2 Analysis of archival dust emission maps

Archival Submillimetre Common-User Bolometer Array 2 (SCUBA-2) data at 850 μm (Mairs et al. 2021) was downloaded from the James Clerk Maxwell Telescope (JCMT) Science Archive to estimate hydrogen column density $N(H_2)$ towards V645 Cyg. Applying the approach by Hildebrand (1983), we used equation (7):

$$N(H_2) = \frac{F_\lambda}{\Omega \mu_{H_2} m_H \kappa_\lambda B_\lambda(T_d)}, \quad (7)$$

where F_λ is the flux in a single beam, Ω is the main beam solid angle (beam area), $\mu_{H_2} = 2.8$ is the mean molecular weight per H_2 molecule, m_H is the mass of atomic hydrogen, κ_λ is the dust opacity per unit mass column density at a given wavelength $\kappa_{850\,\mu m} = 0.01$ cm^2 g^{-1} (Johnstone et al. 2000), B_λ is Planck's law, and the dust temperature in V645 Cyg $T_d = 38$ K (Sandell et al. 2011). We estimated $N(H_2)$ using integrated flux density towards V645 Cyg $S_{850\,\mu m} = 54274$ mJy and the main beam solid angle $\Omega = 4\pi \times (40\ \text{arcsec})^2 = 4.7 \times 10^{-7}$ sr (the main beam size is 40 arcsec). Using equation (5.44) from Tielens (2005), we estimated the UV flux in Habing units, corresponding to the adopted T_d from Sandell et al. (2011).

Table 2. Column densities (N), optical depths (τ), assumed or estimated excitation temperatures (T), and abundances (N/N_{H_2}) of molecules.

Molecule	τ	T (K)	N (cm^{-2})	N/N_{H_2}
CO	<6	38[a]	$(4.6 \pm 0.1) \times 10^{18}$	2.2×10^{-4}
CH_3OH[b]	≤1	≈30[c]	12(0.6–17) $\times 10^{14}$	5.7(2.4–8) $\times 10^{-8}$
CH_3CCH	–	27 ± 2	$(1.4 \pm 0.1) \times 10^{14}$	6.8×10^{-9}
CCH	–	7.9[d]	$(1.4 \pm 0.2) \times 10^{14}$	6.8×10^{-9}
para-H_2CO	–	38[a]	$(5.2 \pm 0.4) \times 10^{14}$	6.5×10^{-9}
HCO^+	7.5 ± 0.1	7.9 ± 0.1	$(1.2 \pm 0.1) \times 10^{14}$	5.9×10^{-9}
HCN	3.8 ± 0.3	7.3 ± 0.1	$(8.4 \pm 0.5) \times 10^{13}$	3.9×10^{-9}
CS	1.0 ± 0.2	7.4 ± 0.4	$(5.6 \pm 0.4) \times 10^{13}$	2.7×10^{-9}
HNC	2.8 ± 0.1	5.9 ± 0.1	$(3.7 \pm 0.2) \times 10^{13}$	1.8×10^{-9}
SO	–	7.9[d]	$(2.2 \pm 0.1) \times 10^{13}$	1.0×10^{-9}
ortho-H_2CS	–	38[a]	$(9.1 \pm 0.9) \times 10^{12}$	3.3×10^{-10}
ortho-c-C_3H_2	–	7.9[d]	$(8.4 \pm 1.2) \times 10^{12}$	3.1×10^{-10}
N_2H^+	<<1	5.9[d]	$(8.3 \pm 0.1) \times 10^{12}$	4.0×10^{-10}
CH_3CHO	–	38[a]	$(4.4 \pm 1.4) \times 10^{12}$	2.1×10^{-10}
HC_3N	–	38[a]	$(3.8 \pm 0.1) \times 10^{12}$	1.8×10^{-10}
SO_2	–	7.9[d]	$(3.4 \pm 0.4) \times 10^{12}$	1.5×10^{-10}
DCO^+	–	7.9[d]	$(2.2 \pm 0.2) \times 10^{12}$	1.0×10^{-10}
HNCO	–	7.9	$(1.6 \pm 0.1) \times 10^{12}$	7.6×10^{-11}
CH_3CN	–	38[a]	$(1.1 \pm 0.2) \times 10^{12}$	5.2×10^{-11}
DNC	–	5.9[d]	$(6.3 \pm 1.3) \times 10^{11}$	3.0×10^{-11}
CCS	–	7.9[d]	$(4.5 \pm 0.4) \times 10^{11}$	2.1×10^{-11}
SiO	–	7.4	$(2.2 \pm 0.4) \times 10^{11}$	1.0×10^{-11}
HCO	–	7.9	$(1.7 \pm 0.6) \times 10^{11}$	8.2×10^{-12}

Note. [a]Dust temperature. [b]Parameters for methanol are taken from non-LTE analysis. [c]Kinetic gas temperature. [d]Excitation temperature of HCO^+.

4 RESULTS

4.1 Detected molecular lines

We detected emission lines of 33 molecules towards V645 Cyg. These lines belong to the different types of molecules, most of them are simple diatomic or triatomic, but there were also detected four COMs: CH_3OH, CH_3CCH, CH_3CHO, and CH_3CN. We present all of the detected lines and their Gaussian approximations in Fig. 1. The detected lines and parameters of their approximation, including integrated intensity of the line $\int T_{mb}\,dv$, radial velocity V_{LSR}, FWHM ΔV, and the line emission peak T_{mb}, are shown in Table 1. We note that the upper state energies E_u of all the lines of the simple molecules are lower than 25 K. For more complex detected molecules, the upper state energies' values are between several K and 82 K. The peaks of the Gaussian profiles fitted to the detected lines lie between −42.13 and −44.7 km s^{-1}. These values lie within ±1 km s^{-1} from $V_{LSR} = -43$ km s^{-1}, which is the velocity of the Class II methanol maser at 6.7 GHz (Reid et al. 2019). FWHMs of the detected lines *vary* from 1.5 to ≈3 km s^{-1}. Using the T_d value, we estimated that thermal linewidth is 0.8 km s^{-1} and found out that all the lines have non-thermal broadening. It is interesting that such COMs as CH_3OH and CH_3CN have linewidths of 2–3 km s^{-1}, but the lines of CH_3CCH and CH_3CHO have only 1.6–2.3 km s^{-1}. It is possible that the lines of these two COMs are formed in different areas around V645 Cyg.

We found blue and red wings in some line profiles. The red wings are seen for $H^{13}CN$ (1–0), CCH (1–0), HNCO (4–3), HCN (1–0), $HN^{13}C$ (1–0), HCO^+ (1–0), $C^{34}S$ (1–2), CS (2–1), and ^{13}CO (1–0) lines. Blue wings are seen for HCO^+(1–0), ^{13}CO(1–0), and CCH(1–0) lines.

4.2 Molecular abundances and physical conditions

We built a rotational diagram (Fig. 2) using four lines of the CH_3CCH 6_K–5_K line series and two lines of the 5_K–4_K line series in order to estimate the gas temperature in the molecular cloud around V645 Cyg. The rotational temperature of CH_3CCH is $T_{rot} = 27 \pm 2$ K and the column density of this molecule is $(1.4 \pm 0.1) \times 10^{14}$ cm^{-2}. The value is approximately 30 per cent lower than the dust temperature $T_d = 38$ K estimated by Sandell et al. (2011). We did not build a rotational diagram for CH_3CN, because of the presence of blending lines and insufficient signal-to-noise ratio.

According to Kalenskii & Kurtz (2016), excitation of the CH_3OH can be out of LTE. Therefore we estimated the CH_3OH physical parameters with a non-LTE analysis using the 12 CH_3OH lines we observed from 84 to 109 GHz. We used intensities of four confidently detected (>3σ) lines and 2σ upper limits for the other eight undetected lines. For the undetected lines we controlled that their model intensities do not exceed the 1σ level given in Table 1.

We found out that the following parameters: $T_k = 30$(10–97) K, $n_{H_2} = 1.0$(0.2–5.6) $\times 10^4$ cm^{-3}, $N_{CH_3OH} = 9.5$(0.5–18.9) $\times 10^{14}$ cm^{-2}, and $N_{CH_3OH}/N_{H_2} = 3.2$(0.01–31.6) $\times 10^{-7}$ correspond to the minimum χ^2 with the 95 per cent confidence intervals (in parenthesis). In addition, the beam filling factor for the methanol emission was varied from 10 to 100 per cent. Despite the fact that the minimum χ^2 was found for $f = 10$ per cent, the 95 per cent confidence interval encompass the full range of the beam filling factor variation. All simulated intensities given by the best-fitting model correspond to the observed lines intensities within rms 2σ (see Fig. 3). The intensity of the transition 5_{-1}–4_0 E at 84.5 GHz is slightly (within 3σ) underestimated. At the same time, the populations of the levels of that transition are inverted with $\tau = -0.05$ in the

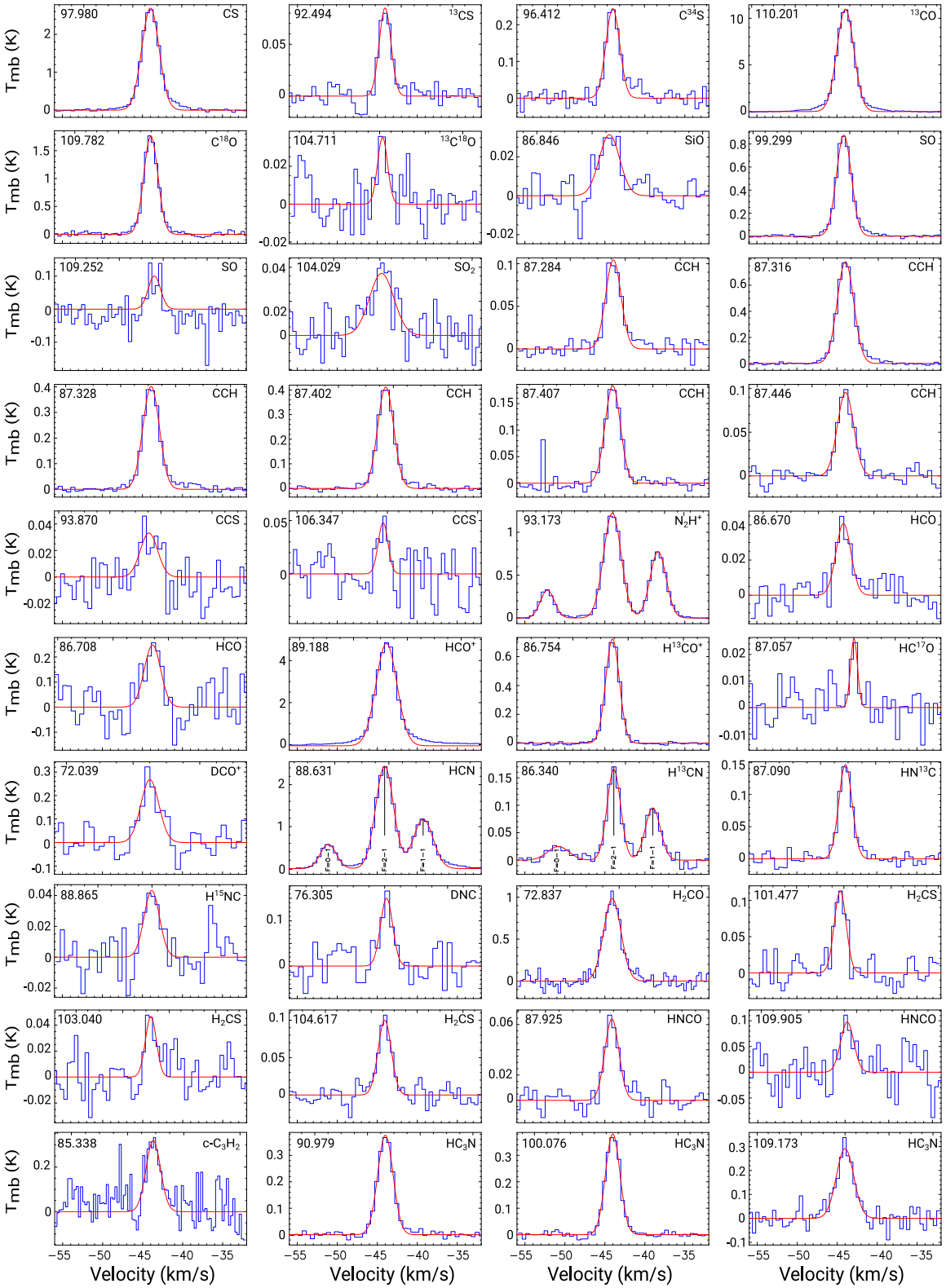

Figure 1. Detected molecular lines with the Gaussian fits. The frequencies of the transitions in GHz are shown at the left upper corner for every particular spectrum.

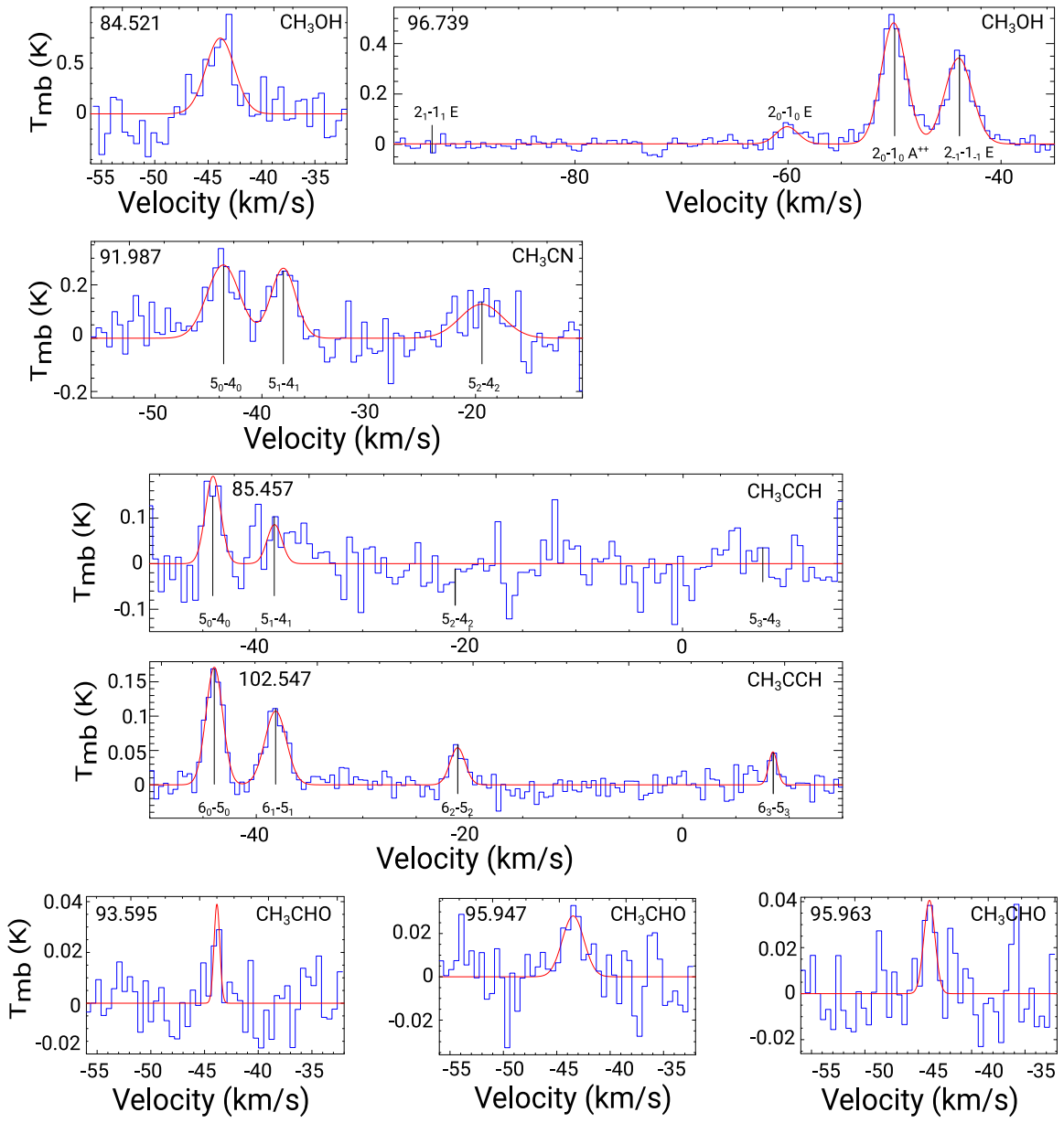

Figure 1. Continued.

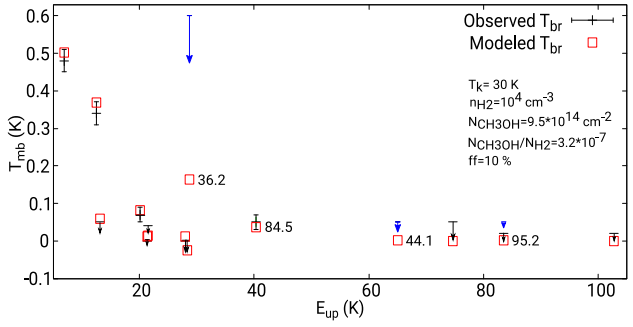

Figure 2. Rotational diagram for CH_3CCH 5_K–4_K and 6_K–5_K line series.

model. Based on this fact, we suppose that maser emission can affect the intensity of the 5_{-1}–4_0 E transition. Populations of the 8_0 and 7_1 A^{++} levels are slightly inverted too ($\tau = -0.01$) and the simulated intensity at 95.169 GHz is lower than 0.02 K in agreement with our observations. We note that the derived T_k value is close to the T_{rot} obtained with the rotational diagram analysis of CH_3CCH lines and agrees within the uncertainties with T_d = 38 K.

We estimated column densities (N) of 23 other molecules using LTE approximation. The N values are given in Table 2, organized from the more to less abundant molecule. It is seen that ^{13}CO(1–0), HCO^+(1–0), CS(2–1), HCN(1–0), and HNC(1–0) lines have moderate optical depths $1 < \tau < 10$, while τ for all the other lines could not be determined. Except for CH_3CCH and methanol, $T_{ex} < 10$ K for species for which we were able to estimate it considering optically thick and thin isotopes. Therefore, excitation of the HCO^+(1–0),

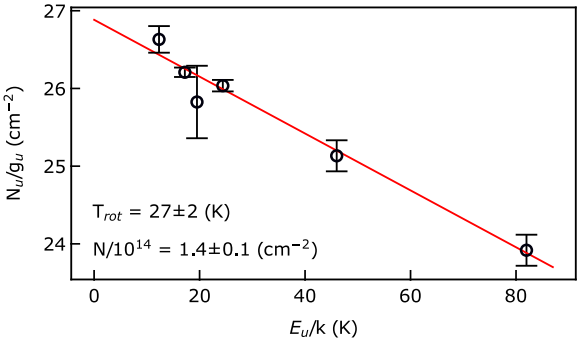

Figure 3. Comparison of the modelled methanol intensities with observed data. Confidently detected transitions, according to Table 1, are marked with error bars, the upper levels of undetected transitions are marked with black arrows. The upper levels of undetected transitions by Liechti & Wilson (1996) and Kim et al. (2018) are marked with blue arrows. The lengths of the arrows are those of the rms values of the corresponding observations.

CS(2–1), HCN(1–0), and HNC(1–0) lines is subthermal as their $T_{ex} < T_d$. If we could not estimate T_{ex} from observations, we used the $T_{ex}(HCO^+) = 7.9$ K for small hydrocarbons, $T_{ex}(HCO^+) = 5.9$ K for small molecules with nitrogen, and $T_{ex} = T_d$ for more complex molecules, respectively (see Table 2).

For the adopted T_d value we estimated column density of molecular hydrogen $N_{H_2} = 2.1 \times 10^{22}$cm^{-2} from the SCUBA-2 dust emission, and used this value to determine relative molecular abundances $x = N/N_{H_2}$, which are also given in the Table 2. The abundances of all the observed molecules, except for CO, H_2CO, and CH_3OH, do to exceed 10^{-8}, the lowest value computed being $<10^{-11}$ for HCO. The measured abundance of CO relative to H_2 molecules gives 1.1×10^{-4} of carbon and oxygen locked in the gas-phase molecules. With the estimated UV flux in Habing units $G0 = 367$, we note that the UV field can be responsible for destruction of complex molecules around V645 Cyg.

4.3 Molecular line emission maps

We show obtained maps of integral intensities of molecular lines emission around V645 Cyg in Figs 4 and 5. For those emission lines, where signal-to-noise ratio allows us to make channel maps, we also show them. We obtained maps of two emission lines of CO isotopologues: ^{13}CO(1–0) and C^{18}O(1–0), two maps of CS isotopologues: CS(2–1) and C^{34}S(2–1), maps of HCO^+(1–0), HCN(1–0), HNC(1–0), N_2H^+(1–0) emission, and also a map of summed methanol emission of three detected lines of 2_K–1_K line series in the [−62, −40] km s^{-1} velocity range.

As we see from all the maps, the bulk of molecular emission is concentrated in the range of radial velocities −47 to −41 km s^{-1} with the peak at the −45 to −43 km s^{-1}. The east–west extension of the cloud, clearly visible at 850 μm dust emission, is also seen on the CH_3OH 2_K–1_K map, while emission of CO, CS, HCO^+, HCN, and HNC is distributed more uniformly around the submm emission peak at 850 μm. We note that the peak emission of CH_3OH and ^{13}CO molecules is shifted to the east from the star by ≈15 arcsec, which corresponds to 0.3 pc at the distance of V645 Cyg. Spatial distribution of N_2H^+(1–0) line emission is extended from north to south perpendicular to the dust ridge. The north-east extension of the mm emission is visible at the blue range of ^{13}CO, CS, HCO^+, and HNC molecular emission −47 to −45 km s^{-1} (the line profile of the HCN(1–0) line does not allow extracting the blue range on the channel maps). The central velocity interval has an emission peak close to the submm peak, and the ^{13}CO emission is elongated to the north-east side of the map. The red velocity range −43 to −41 km s^{-1} of the ^{13}CO, CS, and HNC emission shows an extension in the south-east direction, as the continuum map.

5 DISCUSSION

5.1 Chemical composition of the ambient cloud around the star

Except for CO, H_2CO, and CH_3OH, we obtained low molecular abundances, less than 10^{-8}, towards V645 Cyg. Several types of chemical templates can be considered to explain the molecular composition of the ambient cloud around the star. First, the cloud can represent features of dark molecular cloud, where most of the molecules are present on the dust grains. Secondly, as the cloud contains a source of UV emission, partly it can be a photodissociation region. Moreover, we might expect to find features of a hot core due to the CO bandhead emission, which appears only in the warm (up to several thousands of K) and dense gas, detected by Clarke et al. (2006). Below we discuss the abundances and their ratios associated with the different templates.

Using fig. 9 in Wolfire, Vallini & Chevance (2022), we classify the HNC(1–0), HCN(1–0), and HCO^+(1–0) intensity ratios arising from PDRs, as our values of $\log(HCO^+/HCN) = 0.18$, $\log(HNC/HCN) = -0.34$, and $\log(HNC/HCO^+) = -0.52$ are being in the PDR areas of all these graphs. As shown in Aguado et al. (2017), HNC photodissociates 1.6 times faster than HCN under the O-star radiation field and 2.2 times faster under the local UV interstellar radiation field. V645 Cyg has its own UV radiation and also immersed into some local field, therefore, our obtained abundance ratio is expected.

For CS molecule we estimated relative abundance of 2.7×10^{-9}, which is close to the values, obtained towards PDR (2×10^{-9}) and dense core (2.9×10^{-9}) in Horsehead (Guzmán et al. 2014), and towards PDR 1 in Orion (2.9×10^{-10}) (Johnstone, Boonman & van Dishoeck 2003). According to Beuther et al. (2002), CS abundances for the most of hot cores regardless of their mass have average values higher than 8×10^{-9}.

HCO radical with abundance of 8.2×10^{-12} seems underabundant in comparison with values obtained in other types of environment. This value is two orders of magnitude lower than in PDRs: 8.4×10^{-10} (Horsehead PDR; Guzmán et al. 2014) and 1.7×10^{-10} (the Orion Bar PDR; Cuadrado et al. 2017). As for other dense cores, HCO abundances are $<8 \times 10^{-11}$ in the dark part of the Horsehead (Guzmán et al. 2014) and 2×10^{-11} in B1-b (Cernicharo et al. 2012).

Comparing abundances of H_2CO and CH_3OH we see that their ratio is either ≈1 (if we use the lower limit of the methanol abundance) or methanol is at least twice as abundant as formaldehyde. The observed ratio in V645 Cyg does not agree with the 5:3 ratio observed in the Orion Bar PDR by Cuadrado et al. (2017) but looks more like abundance ratio found in molecular clouds (e.g. Kirsanova et al. 2021b). The HCO to H_2CO abundance ratio also does not agree with the observed PDR by Cuadrado et al. (2017), as our value is several orders of magnitude higher. The abundance ratio $N(CCH)/N(c\text{-}C_3H_2) = 17$ also looks like the one found in molecular clouds (there this ratio varies from 1 to 10; Kirsanova et al. 2021b) rather than the one found in PDRs, where this ratio is a factor of 2

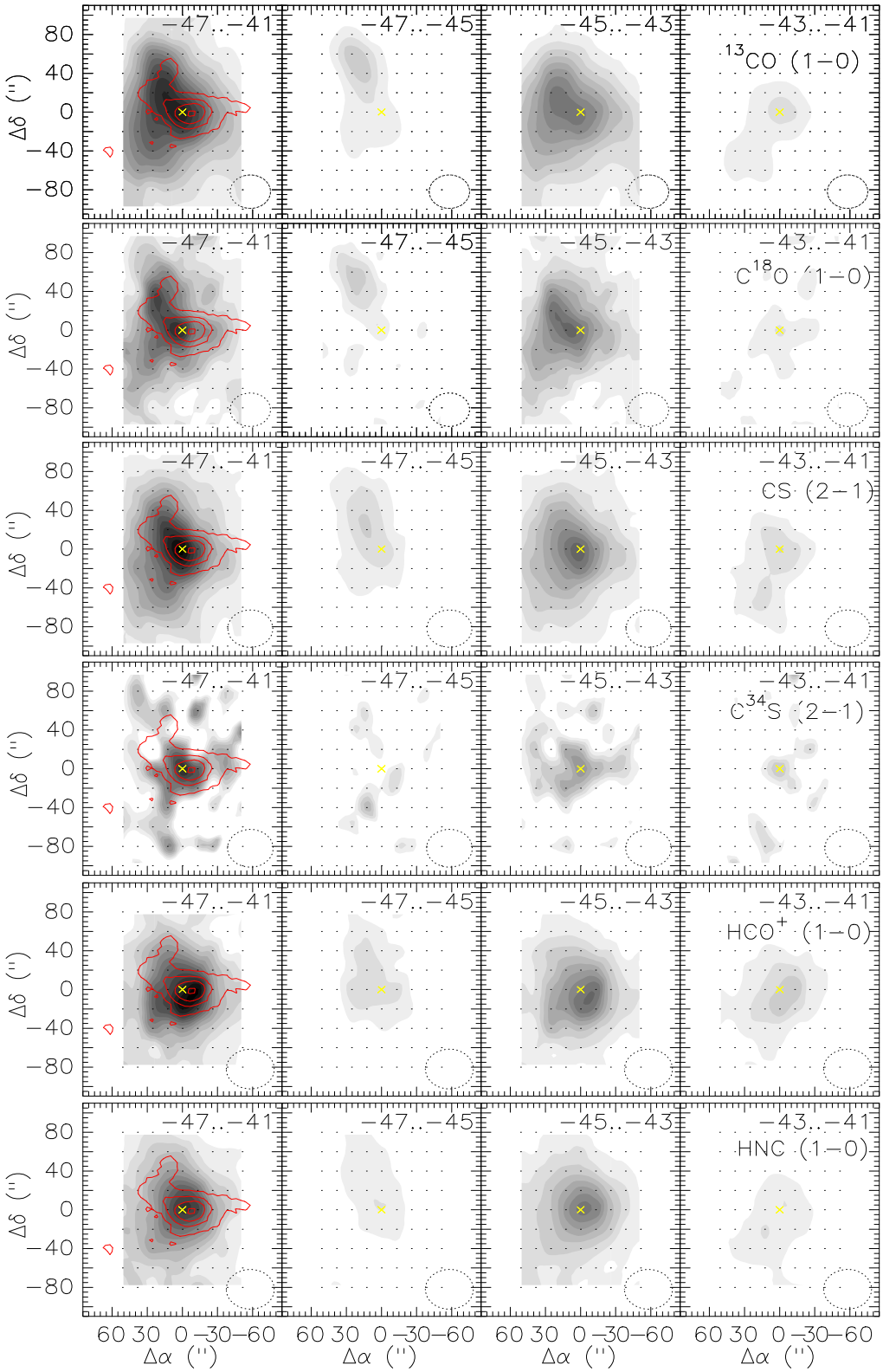

Figure 4. Maps of ^{13}CO(1–0), C^{18}O(1–0), CS(2–1), C^{34}S(2–1), HCO$^+$(1–0), and HNC(1–0) emission in velocity intervals (values of the intervals in km s^{-1} are presented in the top). Grey contours show scale from 30 to 100 per cent of the integral intensities (K km s^{-1}). Emission at 850 μm (Sandell et al. 2011) is shown by red contours. The central position of the map, marked by yellow cross, corresponds to the Class II methanol maser (21:39:58.9, +50:14:24, J2000). The beam size is shown in the bottom right corner of each panel.

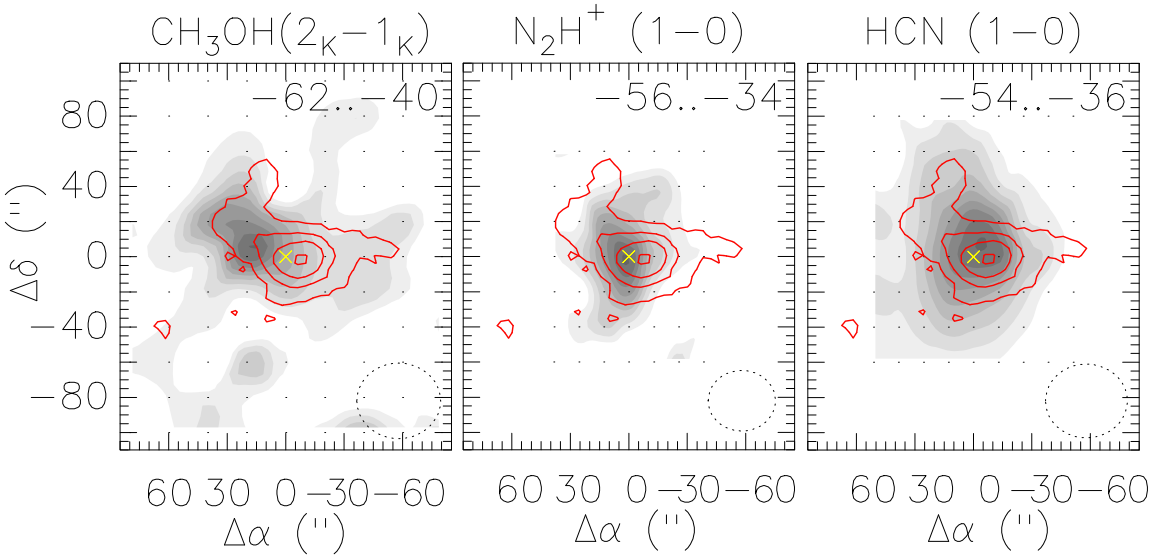

Figure 5. Maps of $CH_3OH(2_K–1_K)$, $N_2H^+(1–0)$, and HCN(1–0) emission in velocity intervals (values of the intervals in km s^{-1} are presented in the top). Grey contours show scale from 30 to 100 per cent of the integral intensities (K km s^{-1}). Emission at 850 μm (Sandell et al. 2011) is shown by red contours. The central position of the map, marked by yellow cross, corresponds to the Class II methanol maser (21:39:58.9, +50:14:24, J2000). The beam size is shown in the bottom right corner of each panel.

higher (e.g. it is about 30 in the Orion Bar PDR; see Cuadrado et al. 2015).

In spite of signatures of dark cloud chemistry in V645 Cyg, we suggest that evaporation of the dust ices is taking place there. The measured N(HNC) from the HNC(1–0)/HN^{13}C(1–0) line ratio is two times less than the value from the HNC(1–0)/H^{15}NC(1–0) line ratio. This discrepancy can be related to the overabundance of ^{15}N in the gas phase caused by preferable evaporation of this isotope from the ices as it was shown by Redaelli et al. (2023). Since the dust temperature value is 38 K toward V645 Cyg, heating of the molecular gas from the stellar source is expected. In the study by Gieser et al. (2021), authors observed V645 Cyg with NOEMA and found that rotation temperatures for molecular lines are up to 150 K in the 10 000 au (0.04 pc) area around the star. This area is 20 times smaller than our beam, it is why most lines we detected have low upper level energies.

All our findings of molecular abundances in different types of objects, taken from the literature, are presented in Table B1. As we can see, lots of molecules have similar abundances in different types of objects, especially in molecular clouds and hot cores. The molecular environment of V645 Cyg shows features present in all types of considered environments, shown in the Table B1.

5.2 Kinematics of the ambient cloud

Our maps cover an area two times larger than the previous observations of the region performed with the 30-m IRAM telescope by Verdes-Montenegro et al. (1991). They found blue and red wings of the ^{13}CO(1–0) emission, observed up to 20 arcsec (approximately 0.4 pc in the plane of the sky) to the north and south, respectively. If we select the same velocity ranges and area as these authors, we see the same behaviour around the centre of the map. However, at larger scale ≈±80–100 arcsec (approximately 1.6–2.0 pc), our ^{13}CO(1–0) channel map shows the opposite behaviour, namely, the blue wing is in the north and the red is in the south. The same velocity structure is seen in our C^{18}O(1–0), CS(2–1), HCO$^+$(1–0), and HNC(1–0) velocity channel maps. To explain this gas kinematics, we suggest that the velocity structures in the immediate vicinity of the star (seen by Verdes-Montenegro et al. 1991, with a spatial resolution 1.5 times higher than our) and in the ambient molecular cloud are not the same.

5.3 Class I methanol maser emission?

As it is well known, methanol masers are empirically divided into two classes, Class I and Class II (Menten 1991). Class I methanol masers are excited by collisions, and are associated with environments of outflow or regions where shock waves pass through, for example, nearby expanding shells of H II regions. Contradictory, Class II methanol masers have predominantly radiative excitation, they are observed around young stellar objects and might be associated with the discs around young massive stars. If Class II methanol masers at 6.7 GHz, also found in V645 Cyg, are detected in the regions of massive stars formation exclusively, Class I masers are registered nearby low massive young stars too (Kalenskii et al. 2010).

According to the maser data base `MaserDb` (Ladeyschikov, Bayandina & Sobolev 2019) and the references therein, Class I methanol maser emissions in V645 Cyg has not been registered yet. Liechti & Wilson (1996) have not detected emission at 36.169 GHz at the Effelsberg 100-m telescope with rms of 0.400 Jy (about 0.6 K). Kim, Kim & Park (2018) have not detected Class I maser emission at 44 and 95 GHz with the Korean VLBI Network (KVN) interferometer at the rms level of 0.7–0.8 Jy (∼0.05 K).

Remarkably, with our best-fitting model described in Section 4.2 and shown in Fig. 3, intensities of the Class I maser transitions at 36.169 and 44.069 GHz are too low to be detected with the rms achieved by Liechti & Wilson (1996) and Kim et al. (2018). According to our model, they could have detected the methanol emission at 84.521 and 95.169 GHz, with better rms observations.

The spectrum at 84.521 GHz has a tiny additional spectral component. If we fit the profile with two Gaussian functions, apart from the main spectral component, we get an additional narrow (0.6 ± 0.2 km s^{-1}) spectral component with $V_{\rm LSR}$ = −42.90 ± 0.01 km s^{-1} (close to the main cloud velocity) and $T_{\rm mb}$ =

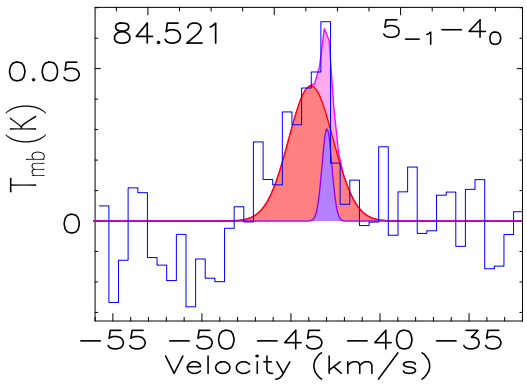

Figure 6. Double Gaussian fit of the 5_{-1}–4_0 E at 84.521 GHz spectral profile (in magenta). Main component Gaussian fit is wider and additional Gauss fit is thinner.

0.03 ± 0.02 K (see Fig. 6). It is known that Class I methanol masers spectral components usually are seen closely to the main cloud velocity and have velocity dispersion no more than 1 km s^{-1} (Menten 1991). Since the 5_{-1}–4_0 E transition at 84.521 GHz is known as a Class I methanol maser transition, and this transition has an inverted level population with our best-fitting model parameters, we suggest that we see the demonstration of a weak maser effect in the additional spectral component.

Values of the estimated physical parameters from the methanol emission are in a good agreement with a Class I-type weak maser effect. We obtained a value of methanol fractional abundance $\geq 10^{-8}$ and, at the same time, not too high kinetic temperature ($\approx$30 K) that is needed to start the dust grain mantle evaporation. The value of T_d in V645 Cyg (39 K) is less than the dust grain mantel methanol evaporation temperature (80 K; e.g. Wiebe et al. 2019). Therefore, our value of methanol relative abundance should be explained with other desorption processes, for example, with destruction of dust grain mantles in shock waves, that are expected in outflow regions. Methanol column density in our model $9.5(0.5\text{–}18.9) \times 10^{14}$ cm^{-2} is high enough ($>10^{15}$ cm^{-2}) to excite the Class I methanol masers (Kalenskii et al. 2010).

Bearing in mind all the facts listed above, we hypothesize that we see the evidence of a weak maser effect in the additional spectral component.

6 CONCLUSIONS

We performed observations of molecular line emission at 3 and 4 mm towards the Herbig Be-type star V645 Cyg. We produced a spectral survey towards position of the 6.7 GHz methanol maser near the star and made maps of emission in several molecules. Our main conclusions are as follows.

(i) We find emission lines of 33 molecules. Most of the lines belong to simple two or three atomic molecules but we also detected four COMs (CH_3OH, CH_3CCH, CH_3CHO, and CH_3CN) up to seven atoms. We estimated column densities and relative abundances of 23 molecules and compared these values with those observed in different astrochemical environments: cold dark clouds, PDRs, hot cores, and discs. We find that the abundances and their ratios agree with the values observed in these types of environments. It is expectable that we have all these types on the line of the sight because the star heats the ambient molecular gas and the dust grains, and also radiate UV photons that also contribute to the molecular content of the source.

(ii) Studying maps of the molecular emission, we find that the molecular cloud at 1.6–2.1 pc scale has different direction of the outflow, in comparison with the inner 0.4 pc around V645 Cyg.

(iii) On the basement of non-LTE model of methanol line emission, we consider that there is a weak maser effect in the additional spectral component of the 5_1–4_0 E methanol line at 84.521 GHz.

ACKNOWLEDGEMENTS

MSK is thankful to the staff of the Onsala Space Observatory, especially to P. Bergman for their help during the 2019 and earlier observation sessions. We are thankful to A. M. Sobolev for his advice to observe V645 Cyg and to anonymous referee for their very relevant corrections. SVS was supported by the Russian Ministry of Science and Higher Education, No. FEUZ-2023-0019.

DATA AVAILABILITY

The data underlying this paper will be shared on reasonable request to the corresponding author.

REFERENCES

Aberfelds A., Bartkiewicz A., Szymczak M., Šteinbergs J., Surcis G., Kobak A., Durjasz M., Shmeld I., 2023, MNRAS, 524, 599
Acke B., van den Ancker M. E., Dullemond C. P., 2005, A&A, 436, 209
Aguado A., Roncero O., Zanchet A., Agúndez M., Cernicharo J., 2017, ApJ, 838, 33
Agúndez M., Marcelino N., Cernicharo J., Roueff E., Tafalla M., 2019, A&A, 625, A147
Amin M. Y., 1998, Ap&SS, 260, 405
Andron I., Gratier P., Majumdar L., Vidal T. H. G., Coutens A., Loison J.-C., Wakelam V., 2018, MNRAS, 481, 5651
Bae J.-H., Kim K.-T., Youn S.-Y., Kim W.-J., Byun D.-Y., Kang H., Oh C. S., 2011, ApJS, 196, 21
Belitsky V. et al., 2015, A&A, 580, A29
Benedettini M., Molinari S., Testi L., Noriega-Crespo A., 2004, MNRAS, 347, 295
Beuther H., Schilke P., Menten K. M., Motte F., Sridharan T. K., Wyrowski F., 2002, ApJ, 566, 945
Beuther H. et al., 2018, A&A, 617, A100
Bisschop S. E., Jørgensen J. K., van Dishoeck E. F., de Wachter E. B. M., 2007, A&A, 465, 913
Błaszkiewicz L., Kus A. J., 2004, A&A, 413, 233
Boger G. I., Sternberg A., 2006, ApJ, 645, 314
Bouscasse L., Csengeri T., Belloche A., Wyrowski F., Bontemps S., Güsten R., Menten K. M., 2022, A&A, 662, A32
Buslaeva A. I., Kirsanova M. S., Punanova A. F., 2021, Astron. Rep., 65, 488
Cazaux S., Tielens A. G. G. M., Ceccarelli C., Castets A., Wakelam V., Caux E., Parise B., Teyssier D., 2003, ApJ, 593, L51
Cernicharo J. et al., 2011, A&A, 531, A103
Cernicharo J., Marcelino N., Roueff E., Gerin M., Jiménez-Escobar A., Muñoz Caro G. M., 2012, ApJ, 759, L43
Clarke A. J., Lumsden S. L., Oudmaijer R. D., Busfield A. L., Hoare M. G., Moore T. J. T., Sheret T. L., Urquhart J. S., 2006, A&A, 457, 183
Cuadrado S., Goicoechea J. R., Pilleri P., Cernicharo J., Fuente A., Joblin C., 2015, A&A, 575, A82
Cuadrado S., Goicoechea J. R., Cernicharo J., Fuente A., Pety J., Tercero B., 2017, A&A, 603, A124
Dickens J. E., Irvine W. M., Snell R. L., Bergin E. A., Schloerb F. P., Pratap P., Miralles M. P., 2000, ApJ, 542, 870
Eisner J. A. et al., 2015, MNRAS, 447, 202
Esplugues G. B. et al., 2013, A&A, 559, A51
Feng S., Beuther H., Semenov D., Henning T., Linz H., Mills E. A. C., Teague R., 2016, A&A, 593, A46

Fuente A., Treviño-Morales S. P., Alonso-Albi T., Sánchez-Monge A., Rivière-Marichalar P., Navarro-Almaida D., 2021, MNRAS, 507, 1886
Giers K. et al., 2023, A&A, 676, A78
Gieser C. et al., 2021, A&A, 648, A66
Girart J. M., Curiel S., Rodríguez L. F., Cantó J., 2002, Rev. Mex. Astron. Astrofis., 38, 169
Goodrich R. W., 1986, ApJ, 311, 882
Gorda S., Bisyarina A., Sobolev A., Parfenov S., 2022, Peremennye Zvezdy, 42, 11
Guzmán V. V., Pety J., Gratier P., Goicoechea J. R., Gerin M., Roueff E., Le Petit F., Le Bourlot J., 2014, Faraday Discussions, 168, 103
Hacar A., Tafalla M., 2011, A&A, 533, A34
Hacar A., Tafalla M., Alves J., 2017, A&A, 606, A123
Hamann F., Persson S. E., 1989, ApJ, 339, 1078
Harju J., Lehtinen K., Booth R. S., Zinchenko I., 1998, A&AS, 132, 211
Hildebrand R. H., 1983, QJRAS, 24, 267
Imai M. et al., 2022, ApJ, 934, 70
Johnstone D., Wilson C. D., Moriarty-Schieven G., Joncas G., Smith G., Gregersen E., Fich M., 2000, ApJ, 545, 327
Johnstone D., Boonman A. M. S., van Dishoeck E. F., 2003, A&A, 412, 157
Juárez C. et al., 2017, A&A, 597, A74
Kalenskii S. V., Kurtz S., 2016, Astron. Rep., 60, 702
Kalenskii S. V., Johansson L. E. B., Bergman P., Kurtz S., Hofner P., Walmsley C. M., Slysh V. I., 2010, MNRAS, 405, 613
Kim C.-H., Kim K.-T., Park Y.-S., 2018, ApJS, 236, 31
Kirsanova M. S., Salii S. V., Kalenskii S. V., Wiebe D. S., Sobolev A. M., Boley P. A., 2021a, MNRAS, 503, 633
Kirsanova M. S., Punanova A. F., Semenov D. A., Vasyunin A. I., 2021b, MNRAS, 507, 3810
Ladeyschikov D. A., Bayandina O. S., Sobolev A. M., 2019, AJ, 158, 233
Larionov G. M., Val'tts I. E., Winnberg A., Johansson L. E. B., Booth R. S., Golubev V. V., 1999, A&AS, 139, 257
Leurini S., Parise B., Schilke P., Pety J., Rolffs R., 2010, A&A, 511, A82
Liechti S., Wilson T. L., 1996, A&A, 314, 615
Liu T., Zhang H., Wu Y., Qin S.-L., Miller M., 2011, ApJ, 734, 22
Lo N., Cunningham M., Bains I., Burton M. G., Garay G., 2007, MNRAS, 381, L30
Mairs S. et al., 2021, AJ, 162, 191
Matthews H. E., Friberg P., Irvine W. M., 1985, ApJ, 290, 609
Menten K. M., 1991, in Haschick A. D., Ho P. T. P., eds, ASP Conf. Ser. Vol. 16, Atoms, Ions and Molecules: New Results in Spectral Line Astrophysics. Astron. Soc. Pac., San Francisco, p. 119
Minh Y. C., Irvine W. M., Brewer M. K., 1991, A&A, 244, 181
Miroshnichenko A. S. et al., 2009, A&A, 498, 115
Molet J. et al., 2019, A&A, 626, A132
Ohishi M., Kaifu N., 1998, Faraday Discussions, 109, 205
Ohishi M., Irvine W. M., Kaifu N., 1992, in Singh P. D., ed., Proc. IAU Symp. 150, Astrochemistry of Cosmic Phenomena. Kluwer, Dordrecht, p. 171
Ohishi M., McGonagle D., Irvine W. M., Yamamoto S., Saito S., 1994, ApJ, 427, L51
Pegues J. et al., 2023, ApJ, 948, 57
Pickett H. M., Poynter R. L., Cohen E. A., Delitsky M. L., Pearson J. C., Müller H. S. P., 1998, J. Quant. Spectrosc. Radiat. Transf., 60, 883
Pomohaci R., Oudmaijer R. D., Goodwin S. P., 2019, MNRAS, 484, 226
Pratap P., Dickens J. E., Snell R. L., Miralles M. P., Bergin E. A., Irvine W. M., Schloerb F. P., 1997, ApJ, 486, 862
Redaelli E., Bizzocchi L., Caselli P., Pineda J. E., 2023, A&A, 674, L8
Reid M. J. et al., 2019, ApJ, 885, 131
Rivilla V. M., Beltrán M. T., Cesaroni R., Fontani F., Codella C., Zhang Q., 2017, A&A, 598, A59
Salii S., Parfenov S., Sobolev A., 2018, in Modern Star Astronomy. IZMIRAN, Moscow, p. 276,
Sandell G., Weintraub D. A., Hamidouche M., 2011, ApJ, 727, 26
Scappini F., Cecchi-Pestellini C., Olberg M., Casolari A., Fanti C., 1998, ApJ, 504, 866
Schöier F. L., Jørgensen J. K., van Dishoeck E. F., Blake G. A., 2002, A&A, 390, 1001
Schreyer K., Helmich F. P., van Dishoeck E. F., Henning T., 1997, A&A, 326, 347
Sewiło M. et al., 2022, ApJ, 931, 102
Shakhvorostova N. N., Alakoz A. V., Bayandina O. S., Olofsson A. O. H., Val'tts I. E., 2023, MNRAS, 526, 1165
Shevchenko V. S., Grankin K. N., Ibragimov M. A., Melnikov S. Y. U., Yakubov S. D., 1994, in The P. S., Perez M. R., van den Heuvel E. P. J., eds, ASP Conf. Ser. Vol. 62, The Nature and Evolutionary Status of Herbig Ae/Be Stars. Astron. Soc. Pac., San Francisco, p. 47
Skinner S. L., Brown A., Stewart R. T., 1993, ApJS, 87, 217
Slysh V. I., Val'tts I. E., Kalenskii S. V., Voronkov M. A., Palagi F., Tofani G., Catarzi M., 1999, A&AS, 134, 115
Slysh V. I., Voronkov M. A., Val'tts I. E., Migenes V., 2002, Astron. Rep., 46, 969
Smirnov-Pinchukov G. V., Moór A., Semenov D. A., Ábrahám P., Henning T., Kóspál Á., Hughes A. M., di Folco E., 2022, MNRAS, 510, 1148
Szymczak M., Hrynek G., Kus A. J., 2000, ApJS, 143, 269
Takano S. et al., 1998, A&A, 329, 1156
Taniguchi K., Herbst E., Ozeki H., Saito M., 2019, ApJ, 884, 167
Thi W. F., van Zadelhoff G. J., van Dishoeck E. F., 2004, A&A, 425, 955
Tielens A. G. G. M., 2005, The Physics and Chemistry of the Interstellar Medium. Cambridge Univ. Press, Cambridge
van der Wiel M. H. D., van der Tak F. F. S., Ossenkopf V., Spaans M., Roberts H., Fuller G. A., Plume R., 2009, A&A, 498, 161
van Dishoeck E. F., Blake G. A., Jansen D. J., Groesbeck T. D., 1995, ApJ, 447, 760
Verdes-Montenegro L., Gomez J. F., Torrelles J. M., Anglada G., Estalella R., Lopez R., 1991, A&A, 244, 84
Wiebe D. S., Molyarova T. S., Akimkin V. V., Vorobyov E. I., Semenov D. A., 2019, MNRAS, 485, 1843
Wilson T. L., 1999, Rep. Progress Phys., 62, 143
Wolfire M. G., Vallini L., Chevance M., 2022, ARA&A, 60, 247
Yang Y.-L. et al., 2020, ApJ, 891, 61
Yang Y., Wang Y., Jiang Z., Chen Z., 2023, MNRAS, 518, 1472

APPENDIX A: UNIDENTIFIED LINES

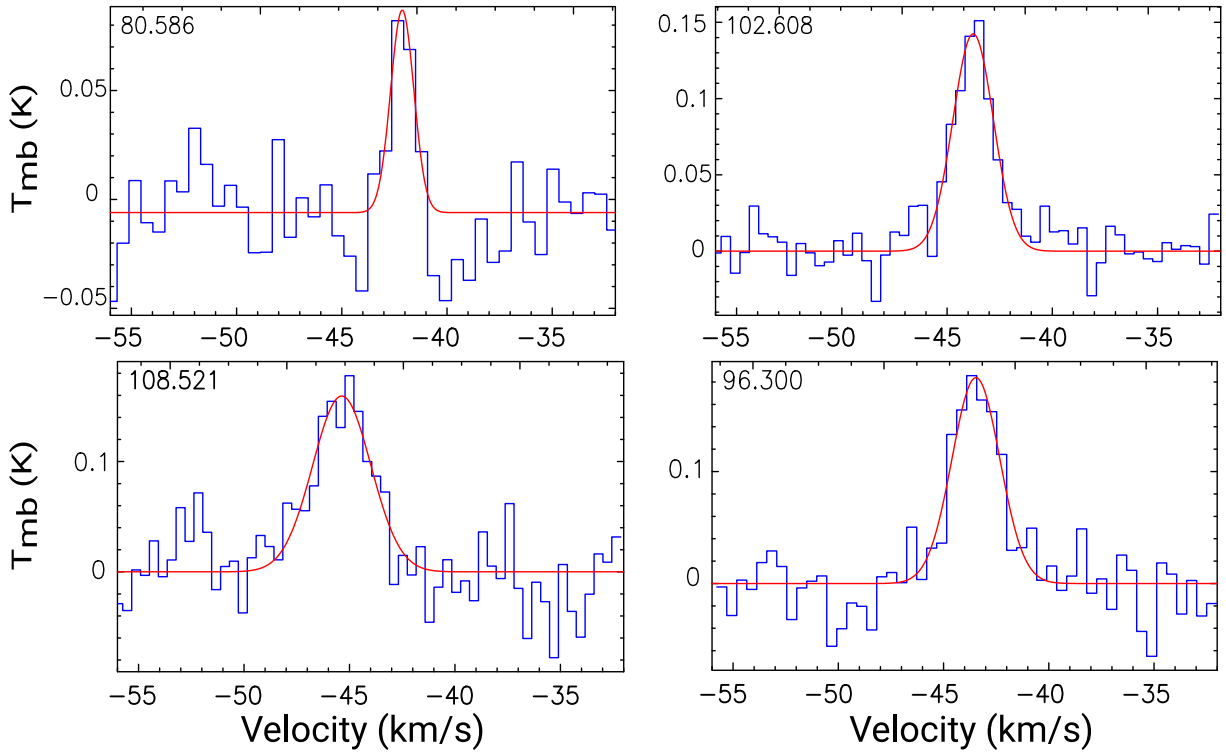

Figure A1. Unidentified emission. The frequencies of the transitions in GHz are shown at the left upper corner for every particular spectrum.

APPENDIX B: ABUNDANCES OF VARIOUS MOLECULES IN DIFFERENT TYPES OF ASTROCHEMICAL ENVIRONMENTS

Table B1 contains our findings about abundances of various molecules in different types of astrochemical environments. We do not pretend to make a full sample because the amount of the literature is too substantial for human search and we believe that some machine learning techniques will help with classifying complex environments of V645 Cyg in the future. All the abundances in the Table B1 are given in units of 10^{-10}.

Table B1. Abundances of various molecules in different types of astrochemical environments

Molecule	V645 Cyg	PDR	Dense core	Starless dense core	Hot core	Hot corino	Molecular cloud	HAe/Be discs
CS	27	20[a], 29[δ]	13[φ], >5.8[ψ]	1.5–40[β]	44[t], 95[υ]	18[o], 30[v]	29[a], 29[e], 9.9[k], 16.5[y]	–
CO	2 200 000	1 100 000[δ]	2 800 000[s], 1 700 000[φ]	400–30000[β]	>58000[t]	–	–	6900[q], 3100[r]
SO	10	10[c]	34.5[ω], 9.2[φ], 50[ψ]	0.6–20[β], 4–20[γ]	380[d], 47[υ], 51[υ]	44[v]	15[e], 57[k], 31.5[y]	–
SO_2	1.5	–	220[ω], 2[φ], 1[ψ]	–	1300[d], 150[o], 82[τ]	160[α], 6.2[v]	3[f], 26[k], <16[y]	–
CCH	68	140[a], 50–100[Ω] 10–20[Λ]	>128[ψ], 20–230[Ω], 7–14[Λ], 25–114[Σ], 20[Γ]	175[η], 61[ζ]	48[υ]	2.1[v]	– –	– –
HCO	0.08	8.4[a]	–	–	–	<2[o]	<0.8[a]	–
HCO+	59	9.0[a]	0.22[φ], >1.7[ψ]	0.5–7[β]	17[υ]	>60[o], 14[v]	39[a], 93[e], 79[k], 119[y]	1[q], 0.078[r]
DCO+	1	–	0.11[φ]	–	0.05[υ]	0.15[o], 0.13[v]	0.8[a]	–
HCN	39	60[c], 40[δ]	32[φ], >6[ψ]	3–20[β]	42[d], 48[υ], 75[λ]	>300[o], 19[o], 11[v]	110[e], 73[k], 115[y]	<0.011[q], <0.091[r]
c-C_3H_2	4	11[a]	52.5[ψ]	–	0.74[ρ], 1.5[τ], 0.5[υ]	6–21[p]	58[g], 20.8[l]	–
N_2H+	4	–	3.6[φ], >15[ψ]	1.5–2.5[θ], 0.4–1.5[γ]	>2.5[t], 4.7[υ]	–	6.8[y]	0.1[q]
H_2CO	260	0.95[a], 14–27[b], 6[c]	206[ω], 9[φ]	0.5[a]	5400[u], 104[t]	8[o], 600[μ]	500[h], 200[m]	<0.14[q], <0.1[r]
H_2CS	4.3	0.8[σ]	–	–	3.3[d], 4.5[λ], 68[λ]	58[α], 1.8–2[v]	10–20[w], 5[x]	–
CH_3OH	570	0.52–0.7[a], 12–16[b]	400[s], 763[ω], 86[φ]	1–1.3[a]	5400[d], 5600[t], 4000[u]	44[o]	32[e], 51[k], 4.3[t], 37.1[y]	<20[q], <1.5[r]
CH_3CCH	29	4.4[a]	23.3[ψ]	3[a]	21[u], 150[υ], <9.9[λ]	2[n]	–	–
CH_3CHO	2.1	0.039–0.14[a]	–	0.2–0.54[a]	<0.47[u], <19[λ], 3.4[υ]	<1[o]	6[i], 6[m]	–
CH_3CN	0.52	2.5[a]	10.5[ω], 0.88[φ]	0.079[a]	1200[u], 72[λ]	80[n], 1.5[o], 100[μ]	6[h], <10[m]	–
HC_3N	1.8	0.063[a]	0.896[ω], <2[φ]	0.079[a], 45[β]	40[z], 5.2[λ], 31[λ]	0.25[o], 1.5[v]	160[j], 4.3[k], 8.7[y]	–

Note. The references for the abundances are following: [a]Horsehead, Guzmán et al. (2014); [b]Orion Bar PDR, Leurini et al. (2010); [c]Orion Bar PDR, van der Wiel et al. (2009); [d]Mon R2 IRS 3, Fuente et al. (2021); [e]TMC–1, Pratap et al. (1997); [f]TMC–1, Cernicharo et al. (2011); [g]TMC–1, Matthews, Friberg & Irvine (1985); [h]TMC–1, Ohishi & Kaifu (1998); [i]TMC-1, Matthews et al. (1985); [j]TMC–1, Ohishi et al. (1994); [k]L134N, Boger & Sternberg (2006); [l]L134N, Takano et al. (1998); [m]L134N, Ohishi, Irvine & Kaifu (1992); [n]IRAS 16293, Andron et al. (2018); [o]IRAS 16293, van Dishoeck et al. (1995); [p]CB 68, Imai et al. (2022); [q]MWC 480, Thi, van Zadelhoff & van Dishoeck (2004); [r]HD 163296, Thi et al. (2004); [s]IRAS 18162−2048, Benedettini et al. (2004); [t]W43-MM1, Molet et al. (2019); [u]NGC 6334 IRS1, Bisschop et al. (2007); [w]TMC–1, Minh, Irvine & Brewer (1991); [x]L134N, Minh et al. (1991); [y]L134N, Dickens et al. (2000); [z]Orion KL, Esplugues et al. (2013), [α]BHR71, Yang et al. (2020); [β]FeSt 1-457, Juárez et al. (2017); [δ]Orion PDR 1, Johnstone et al. (2003); [γ]L1517, Hacar & Tafalla (2011); [ω]NGC 2264 IRS 1, Feng et al. (2016); [ξ]G333.125−0.562, Lo et al. (2007); [φ]NGC 2264 IRS 1, Schreyer et al. (1997); [η]L1521B, Taniguchi et al. (2019); [ζ]L134N, Taniguchi et al. (2019); [θ]Juárez et al. (2017); [κ]Amin (1998); [ψ]L483, Agúndez et al. (2019); [ι]NGC 1333, Hacar, Tafalla & Alves (2017); [μ]IRAS 16293-2422, Cazaux et al. (2003); [ν]IRAS 16293−2422, Schöier et al. (2002); [σ]Orion Bar PDR, Cuadrado et al. (2017); [ρ]N113 A1, Sewiło et al. (2022); [τ]N113 B3, Sewiło et al. (2022); [υ]cold component G328.2551−0.5321, Bouscasse et al. (2022); [λ]warm component G328.2551−0.5321, Bouscasse et al. (2022); [Ω]H II regions S 255 and S 257, Buslaeva, Kirsanova & Punanova (2021); [Λ]S 235, Kirsanova et al. (2021b); [Σ]G109.00+2.73, G121.31+0.64, Yang et al. (2023); [Γ]HH 211, Giers et al. (2023).

This paper has been typeset from a TEX/LATEX file prepared by the author.